AIAA JOURNAL
Vol. 44, No. 12, December 2006

Large-Eddy Simulations of Longitudinal Vortices Embedded in a Turbulent Boundary Layer

Donghyun You* and Meng Wang†
Stanford University, Stanford, California 94305
Rajat Mittal‡
George Washington University, Washington, District of Columbia 20052
and
Parviz Moin§
Stanford University, Stanford, California 94305

DOI: 10.2514/1.22043

Large-eddy simulations of pairs of artificially generated longitudinal vortices embedded in a two-dimensional turbulent boundary layer are performed to study the dynamics of the vortical structures and to provide the unsteady inflow data for use in a future turbomachinery simulation. An immersed boundary method is employed to represent the wall-mounted half-delta wings that generate the counter-rotating vortex pairs. Two vortex pair configurations, with "common flow" between the vortices toward the end wall (common flow down) and away from the end wall (common flow up), respectively, are investigated. Mean velocities and Reynolds stresses compare well with experimental data, demonstrating the accuracy of the numerical approach and, in particular, the efficacy of immersed boundary treatment of the vortex generators. The large coherent vortices are characterized by streamwise velocity defect and negative mean pressure. The boundary layer in the common flow region is thinned by the vortices in the common-flow-down case and thickened by them in the common-flow-up case.

Nomenclature

c	=	Smagorinsky coefficient
f_i	=	x_i component of body force
h	=	height of vortex generator
p	=	pressure
Re	=	Reynolds number
S_{ij}	=	strain rate tensor
T	=	averaging time scale
t	=	time
U	=	time-averaged streamwise velocity
U_∞	=	inflow freestream velocity
u	=	streamwise velocity
u_i	=	x_i component of velocity
u_τ	=	friction velocity
v	=	spanwise velocity
w	=	vertical velocity
x	=	streamwise coordinate
x_i	=	Cartesian coordinates
y	=	spanwise coordinate
z	=	vertical coordinate
Δ	=	grid spacing
ν	=	kinematic viscosity
ρ	=	density
τ_{ij}	=	subgrid-scale stress tensor
$\bar{()}$	=	filtered quantity
$\hat{()}$	=	test-filtered quantity
$()^+$	=	quantity in wall unit
$()'$	=	fluctuation component

Received 25 December 2005; revision received 21 July 2006; accepted for publication 28 July 2006.

*Research Associate, Center for Turbulence Research; dyou@stanford.edu. Member AIAA.

†Senior Research Scientist, Center for Turbulence Research. Currently Associate Professor, Department of Aerospace and Mechanical Engineering, University of Notre Dame. Member AIAA.

‡Associate Professor, Department of Mechanical and Aerospace Engineering. Member AIAA.

§The Franklin P. and Caroline M. Johnson Professor of Engineering, Department of Mechanical Engineering, and Director of Center for Turbulence Research and Center for Integrated Turbulence Simulations. Associate Fellow AIAA.

I. Introduction

LONGITUDINAL vortices embedded in turbulent boundary layers are observed in many flows of practical interest and are sometimes generated on demand for engineering use. Such vortices are often found in pairs, such as the horseshoe vortex produced by a blunt body mounted on the wall. They are sometimes introduced to prevent or delay the boundary-layer separation on an airfoil surface [1] or to reduce the turbulent skin friction [2–4].

On the other hand, the existence of large-scale unsteady vortices, such as those found in the wakes of stator blades mounted on a hub, is also considered a primary factor influencing compressor noise and cavitation in hydraulic pumps. This has motivated recent experiments performed by Kuhl [5] and Ma [6]. They made 3-D laser Doppler anemometer (LDA) [5] and hot-wire [6] measurements of near-wall flows with artificially generated longitudinal vortices, emulating the effect of stator wakes embedded in a turbulent boundary layer upstream of the tip-leakage flow in a linear cascade.

Early studies of longitudinal vortices embedded in turbulent boundary layers have mainly focused on engineering aspects and their use. Pearcy [7] presented a review of measurements for a wide range of vortex arrays and designed vortex generator arrays to forestall boundary-layer separation, but left considerable doubt about how the interaction between the vortices modified their streamwise persistence. Spangler and Wells [8] studied the effects of vortices on local skin friction modification and found that the vortices significantly increased the skin friction at the end wall, where the boundary layer is thinned.

Practical interests in the flow motivated a number of later studies aimed at improving the physical understanding of the interaction between embedded vortices and turbulent boundary layers. Shabaka et al. [9] and Metha and Bradshaw [10] provided a detailed set of data at one streamwise location for each of the two embedded vortex pair

cases, one in which the common flow between the pair was directed toward the wall (common flow down), and the other with the common flow directed away from the wall (common flow up). They made a detailed analysis on the turbulence structure in the disturbed boundary layer. At the same time, Westphal et al. [11] and Pauley and Eaton [12] performed experiments to examine the development of single vortices in both zero and adverse pressure gradients and also the interactions of several vortex pairs embedded in the turbulent boundary layer. They established that the rate of vorticity spreading in a vortex was greatly increased by close proximity of other vortices and provided a correlation between the longitudinal vortices and wall skin friction.

Computational prediction of vortex–boundary layer interaction is difficult with Reynolds-averaged Navier–Stokes (RANS) equations and conventional turbulence models, as mentioned by Shabaka et al. [9]. In addition, the vortex generator imposes a geometric difficulty that traditionally required complex grid topologies. In this study, as an alternative to the conventional methods, large-eddy simulation (LES) is performed using a newly developed solver with the capability of an immersed boundary technique [13]. LES is well suited for studying the detailed dynamics of such flows, because it has the capability of resolving the energy-containing scales temporally as well as spatially. The immersed boundary method allows simulations of flow in complex geometries to be carried out on a simple grid, by assigning body force terms to the momentum equations to enforce the required boundary conditions. This technique has been successfully applied to a variety of complex flows in recent years [13–17].

The objectives of the present study are to demonstrate the capability of LES in conjunction with the immersed boundary technique to accurately and efficiently compute turbulent flow past a vortex generator, to examine the development of longitudinal vortex pairs in a turbulent boundary layer, and to provide the inflow data for simulating the interaction of incoming vortical disturbances with a tip-leakage flow as in the experiment of Ma [6] and as shown in Fig. 1. For this, both configurations of counter-rotating vortices in which the direction of the secondary flow between the vortices can be directed either toward or away from the wall are investigated. Following Metha and Bradshaw [10], they are henceforth referred to as CFD (common flow down) and CFU (common flow up), respectively.

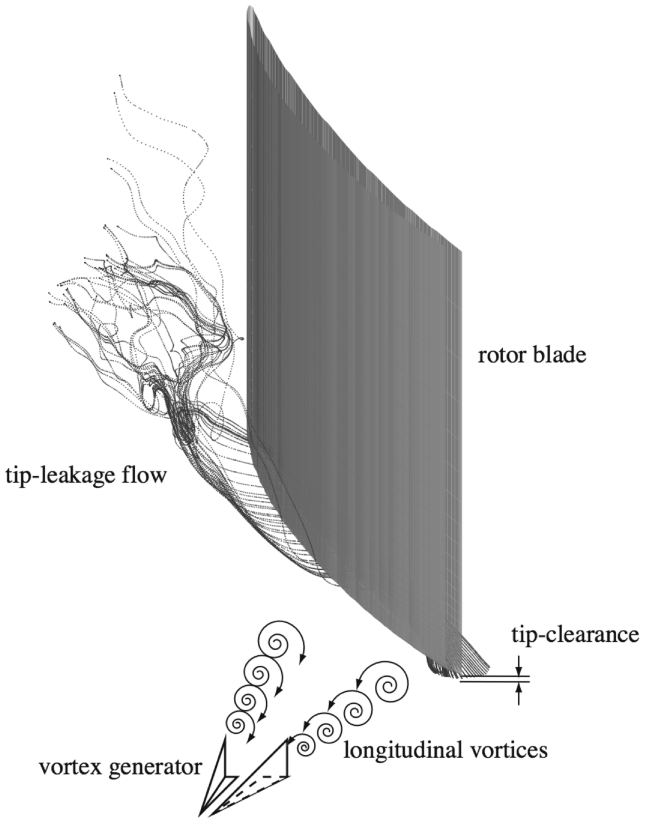

Fig. 1 Flow configuration for studying vortex–rotor interaction.

Computational details and flow configurations are addressed in Sec. II. Discussion of the velocity and pressure fields, along with modifications of the turbulent boundary layer due to the embedded vortices, are given in Sec. III, followed by a summary in Sec. IV.

II. Computational Details

A. Numerical Method

The numerical algorithm and solution methods are described in detail in [18] and the main features of the methodology are summarized here. The spatially filtered Navier–Stokes equations for resolved scales in LES are

$$\frac{\partial \bar{u}_i}{\partial t} + \frac{\partial}{\partial x_j}\bar{u}_i\bar{u}_j = -\frac{\partial \bar{p}}{\partial x_i} + \frac{1}{Re}\frac{\partial}{\partial x_j}\frac{\partial \bar{u}_i}{\partial x_j} - \frac{\partial \tau_{ij}}{\partial x_j} \tag{1}$$

$$\frac{\partial \bar{u}_i}{\partial x_i} = 0 \tag{2}$$

All the coordinate variables, velocity components, and pressure are nondimensionalized by h, U_∞, and ρU_∞^2, respectively. The time is normalized by h/U_∞. The governing Eqs. (2) and (3) are rewritten in a conservative form in generalized coordinates. The key feature of the numerical method is the use of a nondissipative, central-difference spatial discretization scheme that has been demonstrated to be crucial for retaining the accuracy and predictive capability of the LES approach [19].

The subgrid-scale (SGS) stress tensor is modeled by a Smagorinsky-type eddy-viscosity model:

$$\tau_{ij} - \frac{1}{3}\delta_{ij}\tau_{ij} = -2c\Delta^2|\bar{S}|\bar{S}_{ij} \tag{3}$$

Given that the flow is fully three-dimensional with no homogeneous directions, the Lagrangian dynamic SGS model [20] is employed in order to compute c. The Lagrangian dynamic model averages the model coefficient along the flow path lines and therefore does not require a homogeneous direction [21]. The equation for computing the coefficient is

$$c^2(\boldsymbol{x}, t) = \frac{\Phi_{\mathrm{LM}}}{\Phi_{\mathrm{MM}}} \tag{4}$$

where

$$\begin{aligned}\Phi_{\mathrm{LM}} &= \frac{1}{T}\int_{-\infty}^{t} L_{ij}M_{ij}[\boldsymbol{z}(t), t']e^{-(t-t')/T}\,\mathrm{d}t' \\ \Phi_{\mathrm{MM}} &= \frac{1}{T}\int_{-\infty}^{t} M_{ij}M_{ij}[\boldsymbol{z}(t), t']e^{-(t-t')/T}\,\mathrm{d}t'\end{aligned} \tag{5}$$

and L_{ij}, M_{ij}, and $\boldsymbol{z}$ are defined with u_i, Δ, and S_{ij}, as follows:

$$\begin{aligned}L_{ij} &= \widehat{\bar{u}_i\bar{u}_j} - \hat{\bar{u}}_i\hat{\bar{u}}_j, \qquad M_{ij} = 2\Delta^2\left(\widehat{|\bar{S}|\bar{S}_{ij}} - 4|\hat{\bar{S}}|\hat{\bar{S}}_{ij}\right) \\ \boldsymbol{z}(t') &= \boldsymbol{x} - \int_{t'}^{t}\bar{\boldsymbol{u}}[\boldsymbol{z}(t''), t'']\,\mathrm{d}t''\end{aligned} \tag{6}$$

The integration method used to solve the transformed governing equations is based on a fully implicit fractional step method that avoids the severe time-step restriction that would occur in the vortex generator region. All terms, including cross-derivative diffusion terms, are advanced using the Crank–Nicolson method in time and are discretized by the second-order central difference in space. A Newton iterative method is used to solve the discretized nonlinear equations. A highly efficient multigrid procedure is employed to solve the Poisson equation for pressure. The code is parallelized using OpenMP for shared-memory platforms.

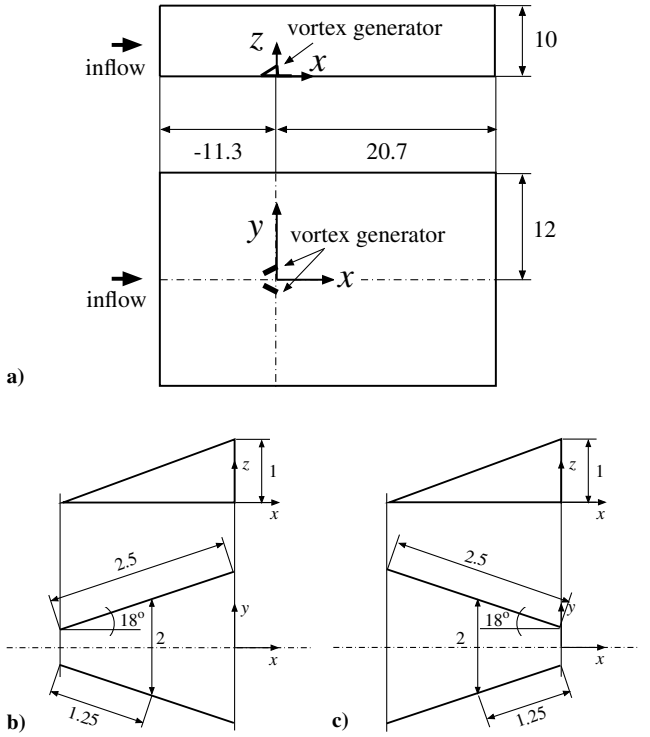

Fig. 2 Flow configuration and coordinate system: a) overall view, b) vortex generator for the CFD case, and c) vortex generator for the CFU case.

B. Flow Configuration

The flow configuration and coordinate definitions for the numerical simulation are schematically shown in Fig. 2. The vortex generators are symmetric pairs of thin half-delta-wings (see Figs. 2b and 2c), which are difficult to resolve using a conventional body-fitted mesh topology. To overcome this difficulty, an immersed boundary technique [13] is used (see Sec. II.C for details).

The computational domain is of size $L_x \times L_y \times L_z = 32h \times 24h \times 10h$. In this domain, both CFD and CFU configurations are simulated, whereas only the CFD situation has been studied in Kuhl's experiment [5], of which results are compared with those from the present LES.

Inflow/outflow boundary conditions are applied in the streamwise direction and no-slip conditions are applied to the bottom wall and side boundaries (see Fig. 2 for the coordinate system). In the upper boundary, a no-stress boundary condition is applied [22]. The inflow is a turbulent boundary layer at a Reynolds number of 700, based on the momentum thickness and generated by using an inflow generation technique of Lund et al. [23]. For the outflow, a convective boundary condition is used, in which the convection speed is set equal to the mean streamwise velocity integrated across the exit plane.

Other important parameters for the simulation are as follows: the span of half-delta-wing is $2.5h$ and the midspan distance between the wings is $2h$. The skew angle of the wing for both diverging (CFD) and converging (CFU) configurations is 18 deg (see Figs. 2b and 2c for schematic diagrams). The Reynolds number of both configurations is 130,000, based on the vortex generator height and inflow freestream velocity.

C. Immersed Boundary Method

The vortex generator configuration poses a considerable challenge for the grid topology. In recent years, the immersed boundary method has emerged as a flexible and efficient tool for treating boundary conditions in complex and/or moving geometries [13,15–17]. With this approach, the simulations can be carried out on a simple grid (see Figs. 3a and 3b illustrating an example of grid assignment in a vortex generator configuration), and boundary conditions are assigned by

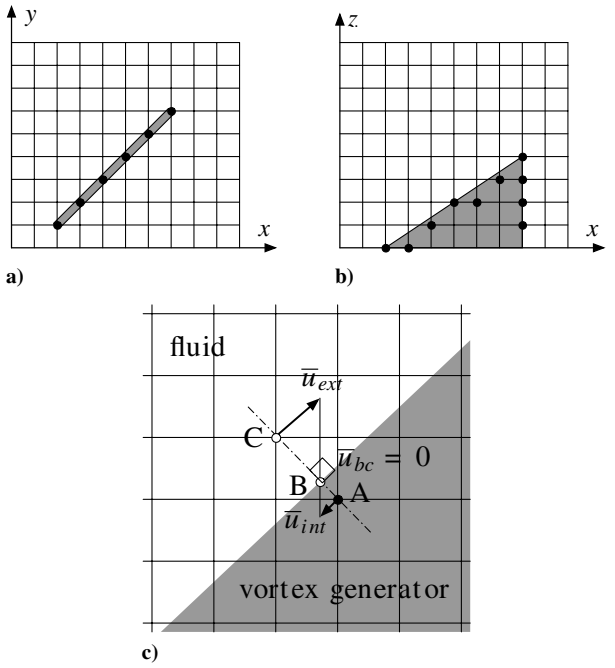

Fig. 3 Example of body forcing in the immersed boundary. A body force is assigned to point A using velocity $\bar{u}_{\text{int}}$, which is extrapolated from the velocities at B ($\bar{u}_{bc}$) and C ($\bar{u}_{\text{ext}}$). The ● represents the location where the body force is assigned.

applying body forces to the momentum equations to mimic the effect of the boundary:

$$f_i^n = \frac{(\bar{u}_{i(\text{desired})} - \bar{u}_i)^n}{\Delta t} + \frac{\partial}{\partial x_j}(\bar{u}_i \bar{u}_j)^n + \frac{\partial \bar{p}^n}{\partial x_i} - \frac{1}{Re}\frac{\partial}{\partial x_j}\frac{\partial \bar{u}_i^n}{\partial x_j} + \frac{\partial \tau_{ij}^n}{\partial x_j} \tag{7}$$

Figure 3c shows an example of body force assignment. Applying a linear or bilinear interpolation technique to point C of outside velocity $\bar{u}_{\text{ext}}$, and to B of boundary velocity (e.g., zero in Fig. 3), the velocity inside of the boundary at A ($\bar{u}_{\text{int}}$) can be estimated. Using this estimation and Eq. (7), the desired body force at point A is obtained.

Grid lines are clustered around the vortex generators for an accurate prediction of flow separation at the edges of the vortex generators, which is crucial in the present study. On the other hand, a change in the grid resolution for predicting attached flow on the vortex generator surfaces makes only a marginal difference. Figure 4 shows the dominant vortex structures in terms of instantaneous

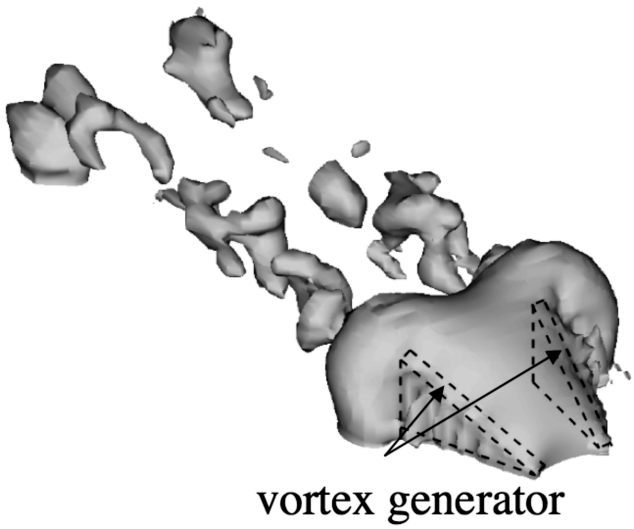

Fig. 4 Instantaneous isosurfaces of $p/\rho U_\infty^2 = -0.01$.

isosurfaces of negative pressure, computed using an immersed boundary representation of the vortex generators. The feasibility of this methodology has been established in a number of canonical flow simulations and in LES of a high Reynolds-number rotor tip-clearance flow [14,18].

III. Results and Discussion

Four simulations have been performed on nonuniform Cartesian meshes of sizes $131 \times 97 \times 97$ ($x \times y \times z$) (mesh 1) and $197 \times 129 \times 129$ (mesh 2) for both CFD and CFU cases. Unless indicated otherwise, the results to be shown next are obtained with mesh 2. Various diagnostics for the mesh quality, such as stretching ratio and mesh aspect ratio, have been carried out in the construction of the final meshes. Grid lines are clustered around the vortex generator, end wall, and wake regions to ensure appropriate resolution.

For the $197 \times 129 \times 129$ mesh, the grid spacings based on the wing height in the streamwise, spanwise, and vertical directions are

$$8.5 \times 10^{-3} \leq \Delta x/h \leq 2.5 \times 10^{-1}$$

$$9 \times 10^{-3} \leq \Delta y/h \leq 6 \times 10^{-1}$$

and

$$2 \times 10^{-3} \leq \Delta z/h \leq 1.6 \times 10^{-1}$$

respectively. In wall units, the end-wall resolution in the region of primary interest for both CFD and CFU cases on mesh 2 is within the range $\Delta x^+ \leq 47$, $\Delta y^+ \leq 33$, and $\Delta z^+ \leq 1.2$. As seen in the following comparisons of the results obtained from simulations employing mesh 1 and mesh 2, the results are reasonably grid-independent.

The simulations are advanced in time with a maximum Courant–Friedrichs–Lewy (CFL) number equal to two, which corresponds to $\Delta t U_\infty/h \approx 0.09$ on mesh 2. Each time step requires a wall clock time of about 26 s when 8 CPUs of an IBM p690 are used. The flow statistics are collected over a time interval of about $100h/U_\infty$.

Gross features of the counter-rotating longitudinal vortex pairs embedded in the turbulent boundary layer are shown in Figs. 5 and 6, which contain instantaneous and time-averaged streamwise velocity contours in a number of y–z planes along the streamwise direction. In both the CFD and CFU cases, the vortex pairs are identified as regions of streamwise velocity deficits. In the CFD situation, as the two longitudinal vortices convect downstream, they move away from each other and toward the end wall (Fig. 5). In contrast, in the CFU case, while the vortices convect downstream, they move away from the end wall and approach each other and eventually are merged in further downstream locations (Fig. 6).

The end-wall boundary layer in the common flow region (region between the vortices) is significantly affected by the vortex pair. The vortex pair in the CFD case increases the end-wall velocity gradients by directing the common flow toward the end wall (Fig. 5). In

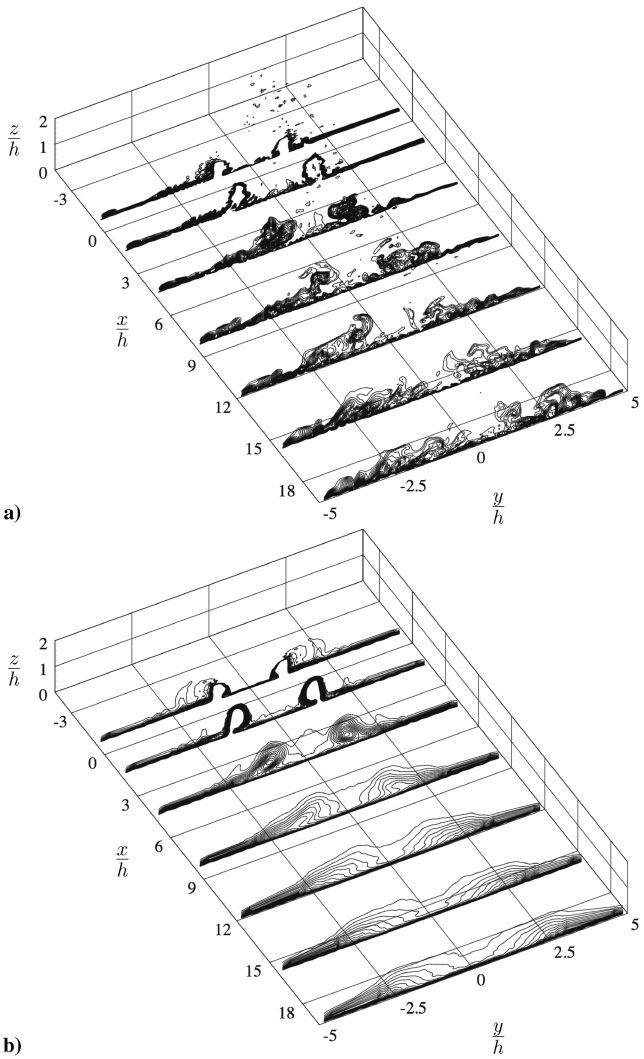

Fig. 5 Streamwise velocity contours for the CFD case in y–z planes along the streamwise direction: a) instantaneous and b) time-averaged. Fourteen contour levels from 0.5 to 0.99 are shown in each plane.

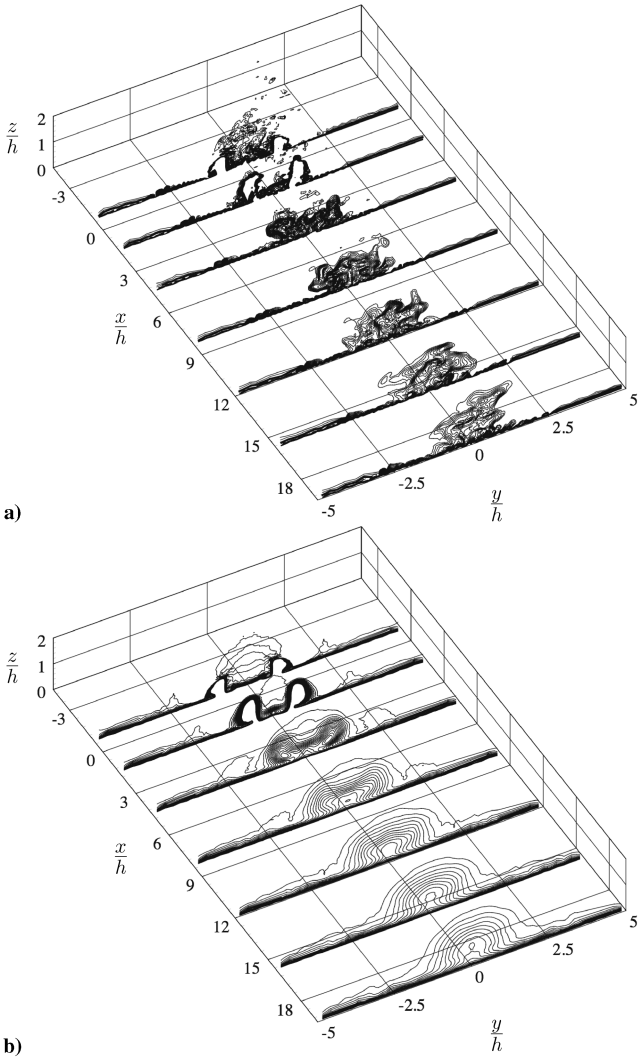

Fig. 6 Streamwise velocity contours for the CFU case in y–z planes along the streamwise direction: a) instantaneous and b) time-averaged. Fourteen contour levels from 0.5 to 0.99 are shown in each plane.

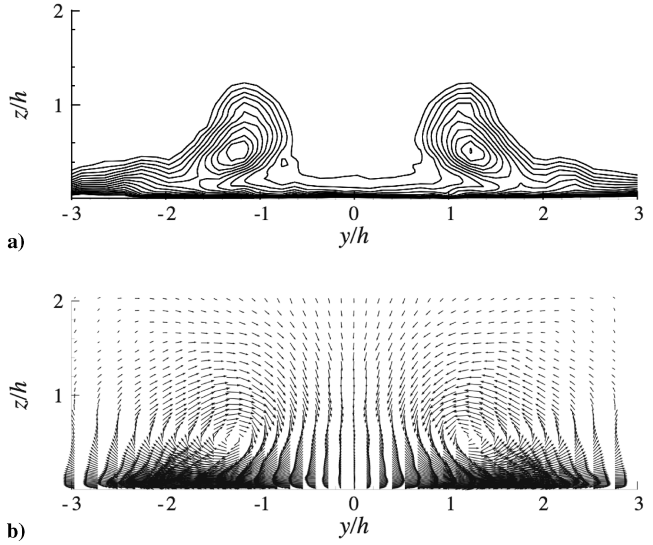

Fig. 7 The CFD case in a y–z plane at $x/h = 5$: a) mean streamwise velocity and b) velocity vectors. Fourteen contour levels in the range of $0.5 \sim 0.99$ are shown for the mean streamwise velocity.

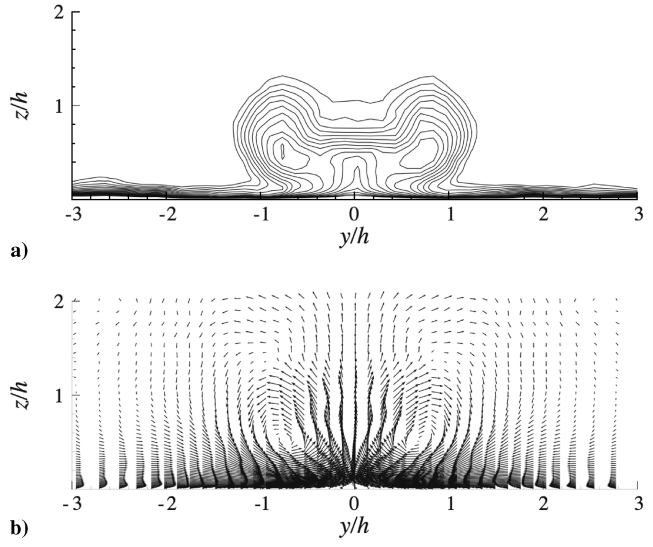

Fig. 8 The CFU case in a y–z plane at $x/h = 5$: a) mean streamwise velocity and b) velocity vectors. Fourteen contour levels in the range of $0.5 \sim 0.99$ are shown for the mean streamwise velocity.

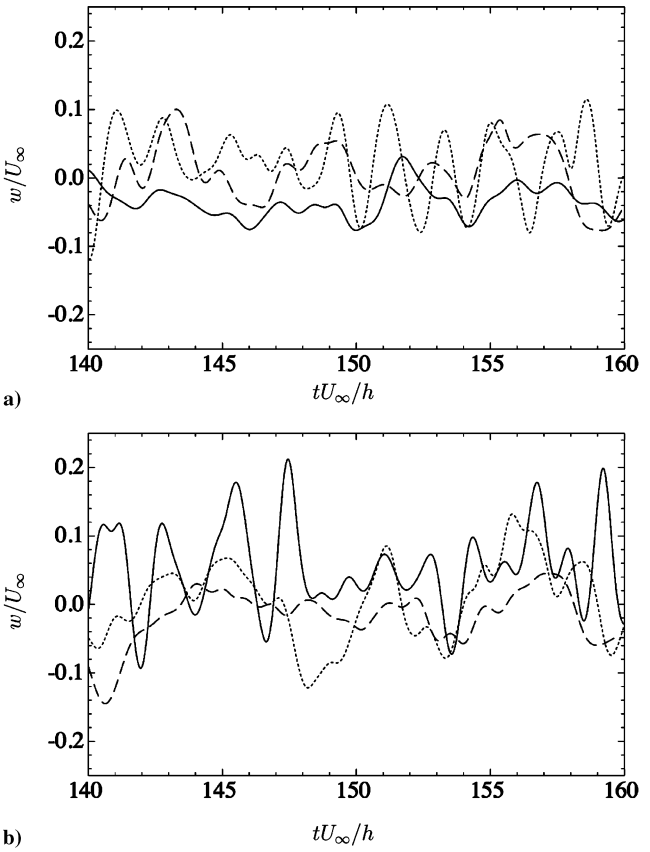

Fig. 9 Time histories of the vertical velocities w/U_∞: a) CFD and b) CFU. A solid line indicates $x/h = 10.5$ and $y/h = 0$ $z/h = 1.1$; a dashed line indicates $x/h = 10.5$, $y/h = -2$, and $z/h = 1.1$; a dotted line indicates $x/h = 10.5$, $y/h = 2$, and $z/h = 1.1$.

contrast, the velocity gradients between the vortex pair decrease by the upward flow motion in the CFU case (Fig. 6). By those mechanisms, the wall skin friction in the common flow region increases (decreases) in the CFD (CFU) case. The same observations have also been reported in a number of experiments [8–12].

Detailed flow characteristics are examined in Figs. 7 and 8, which show the mean streamwise velocity contours and mean velocity vectors in a y–z plane at $x/h = 5$. As shown in Fig. 7, the vortex pair in the CFD case noticeably decreases the boundary-layer thickness in the common flow region and generates strong rotating motions. The CFU vortex pair entrains fluid from the end-wall boundary layer to the middle of the vortex pair, as shown in Fig. 8, and thereby increases the boundary-layer thickness in the common flow region. At $x/h = 5$, the boundary-layer thickness in the middle of the vortex pairs compared with the values at a location away from the vortex pairs decreases 16.7% and increases 450% for CFD and CFU cases, respectively.

Figures 9a and 9b show time histories of the end-wall normal velocities (w/U_∞) found inside and outside of the common flow region. The characteristics of the common flows in both the CFD and CFU cases are clearly discriminated in those figures. In the CFD configuration, the vertical velocity in the middle of the vortex pair is usually directed downward and its fluctuation is, in general, smaller than those found in the vortical regions (solid line in Fig. 9a). However, in the CFU case, the opposite behavior of the vertical velocity in the common flow region is observed in terms of the direction and magnitude of its fluctuation (solid line in Fig. 9b).

Quantitative comparisons have been made between the LES results and experimental measurements in a downstream location, as shown in Figs. 10–12. In the experiment [5], LDV measurements for the CFD configuration were taken to obtain detailed velocity and turbulence statistics. Figure 10 shows mean velocity components in the CFD case along the y direction at a location of $x/h = 10.5$ and $z/h = 0.75$. In general, the LES and experimental results in the CFD case are matched reasonably well (Fig. 10a), and simulations employing two different resolutions (mesh 2 and mesh 1) are also in reasonable agreement in both flow configurations. As shown in Fig. 10a), in the CFD configuration, the streamwise velocity exceeds the freestream velocity in the common flow region, whereas a streamwise velocity deficit and variations of cross-velocity components are clearly noticeable around the core of the longitudinal vortices ($-2 \le y/h \le -1$ or $1 \le y/h \le 2$). On the other hand, flow in the CFU configuration shows a reduced streamwise velocity in the common flow region (Fig. 10b).

Figure 11 shows the mean streamwise velocity profiles normalized by the local friction velocity. In an upstream location from the vortex generator, $x/h = -1.92$, the mean streamwise velocity profile predicted by the present LES (dashed/dotted line in Fig. 11a) is in good agreement with experimental data (circle in Fig. 11a) in the CFD case [5]. In the CFU case, the LES result (dashed/dotted line in Fig. 11b) deviates from the experimental profile for the CFD case (circle in Fig. 11b), especially in the log layer (note that experimental data are only provided in the CFD case). This suggests that the flowfield at this upstream location is affected by the

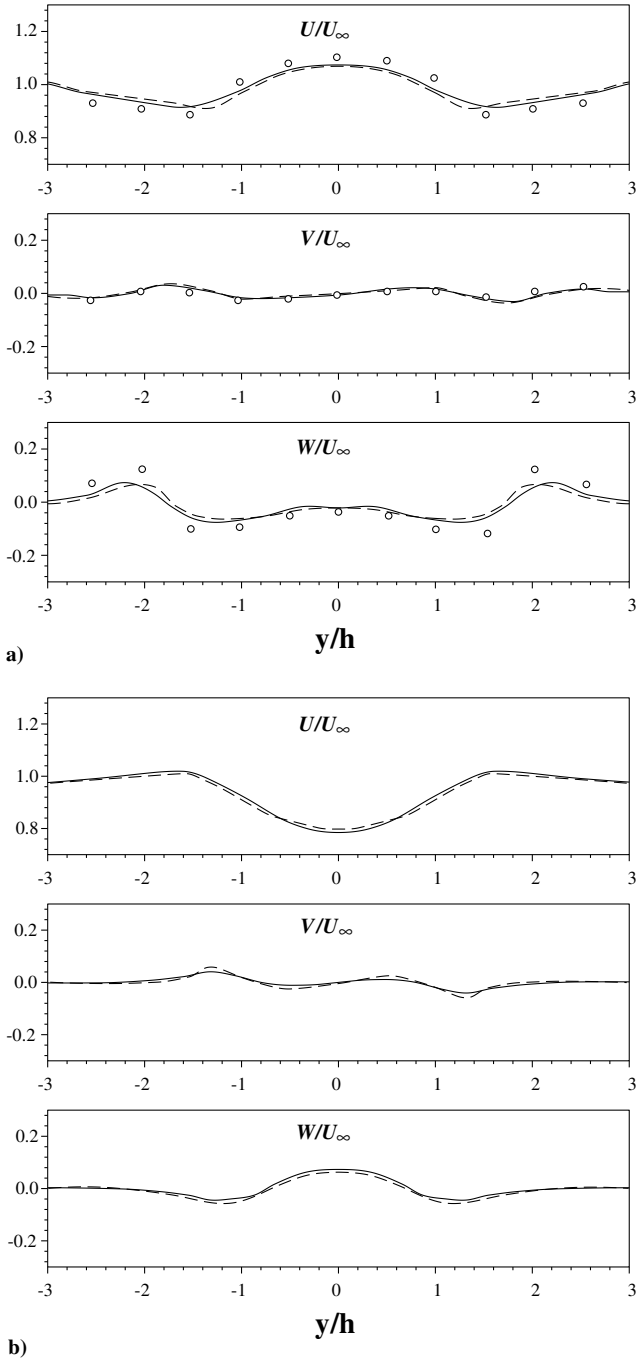

Fig. 10 Profiles of mean velocity components along the y direction at the location of $x/h = 10.5$ and $z/h = 0.75$: a) CFD and b) CFU. A solid line indicates mesh 2 and a dashed line indicates mesh 1. Symbols are from the experiment [5].

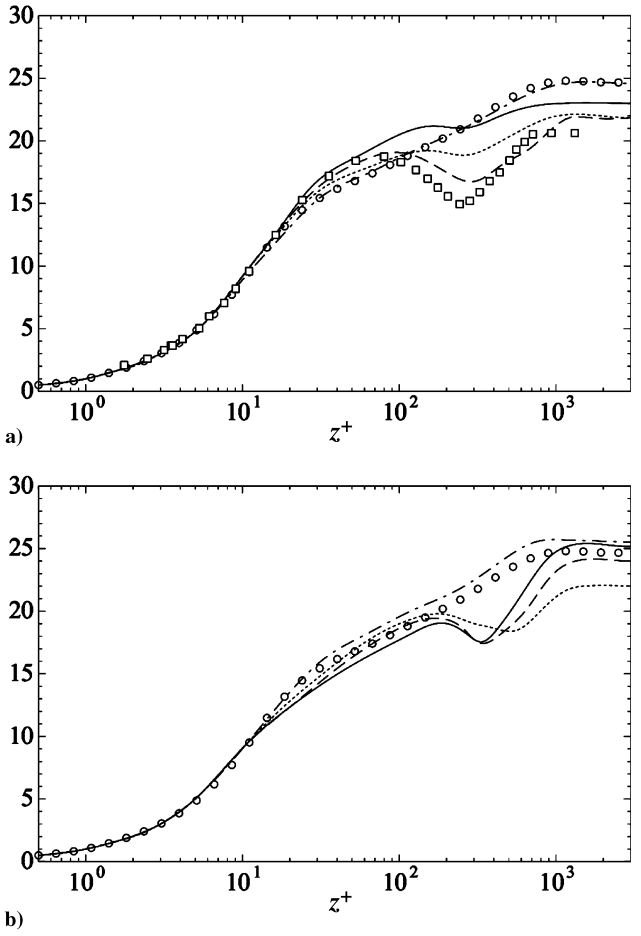

Fig. 11 Profiles of streamwise velocities normalized by the local friction velocity along the z axis: a) CFD and b) CFU. Lines are from the present LES and symbols are from the experiment [5]. A solid line indicates $x/h = 10.5$ and $y/h = 0$; a dashed line and a square indicate $x/h = 10.5$ and $y/h = 1.5$; a dotted line indicates $x/h = 10.5$ and $y/h = 0.5$; and a dotted/dashed line and a circle indicate $x/h = -1.92$ and $y/h = 0$.

downstream vortex generator. The effect of the downstream vortex generator on the upstream flowfield at $x/h \leq -2.5$ was found to be negligible. Vortices significantly influence the log layers in both the CFD and CFU cases downstream of the vortex generators, as exemplified by the velocity defects at $x/h = 10.5$ (Figs. 11a and 11b). In the CFD case, the profile at $x/h = 10.5$ and $y/h = 1.5$ (vortex core) is compared with experimental data. A reasonable agreement is observed in the inner layer, whereas a small deviation is shown in the defect region (dashed line and square in Fig. 11a). In this case, the velocity profile along $y/h = 0$ (in symmetry plane) does not show a large defect, but nonetheless is affected by the vortex pair (solid line in Fig. 11a). Compared with the CFD case, the CFU configuration shows smaller variations in velocity defects at the three y locations and the peak defects are found at locations further away from the wall (Fig. 11b). In the lower log layer, the CFD case shows slightly accelerated profiles, whereas decelerated profiles are observed in the CFU case.

Associated with longitudinal vortex pairs are significant turbulent fluctuations. Figures 12 and 13 show the profiles of Reynolds stresses along the spanwise direction at $x/h = 10.5$ and $z/h = 0.75$ in both the CFD and CFU cases. In general, the simulations employing mesh 1 and mesh 2 show reasonable grid independence in the turbulence statistics. As seen in Fig. 12, the LES results are also in favorable agreement with the experimental data. In the CFD configuration, Fig. 12a shows that the regions of high streamwise velocity deficit ($-2 \leq y/h \leq -1$ and $1 \leq y/h \leq 2$, see Fig. 10a), in which the longitudinal vortices are located, attain peak magnitudes for all Reynolds normal stresses. Their peak values are in the order of spanwise ($\overline{v'v'}$), streamwise ($\overline{u'u'}$), and vertical ($\overline{w'w'}$) velocity components. The vortical structures also generate significant Reynolds shear stresses, as shown in Fig. 12b.

On the other hand, the Reynolds stresses are concentrated near the centerline common flow region in the CFU case ($-1 \leq y/h \leq 1$ in Fig. 13) at $x/h = 10.5$ and $z/h = 0.75$, because the two vortices are nearly merged (cf. Fig. 6). The spanwise Reynolds normal stress $\overline{v'v'}$ achieves the highest peak magnitude, as is also observed in the CFD case. However, the peak magnitude of $\overline{u'u'}$ is smaller than that of $\overline{w'w'}$, in contrast to the CFD case (Fig. 13a). In general, the peak magnitudes of Reynolds normal stresses in the CFU case are higher than those in the CFD case (Figs. 12a and 13a), whereas the magnitudes of Reynolds shear stresses in the CFU case are smaller than those in the CFD case (Figs. 12b and 13b).

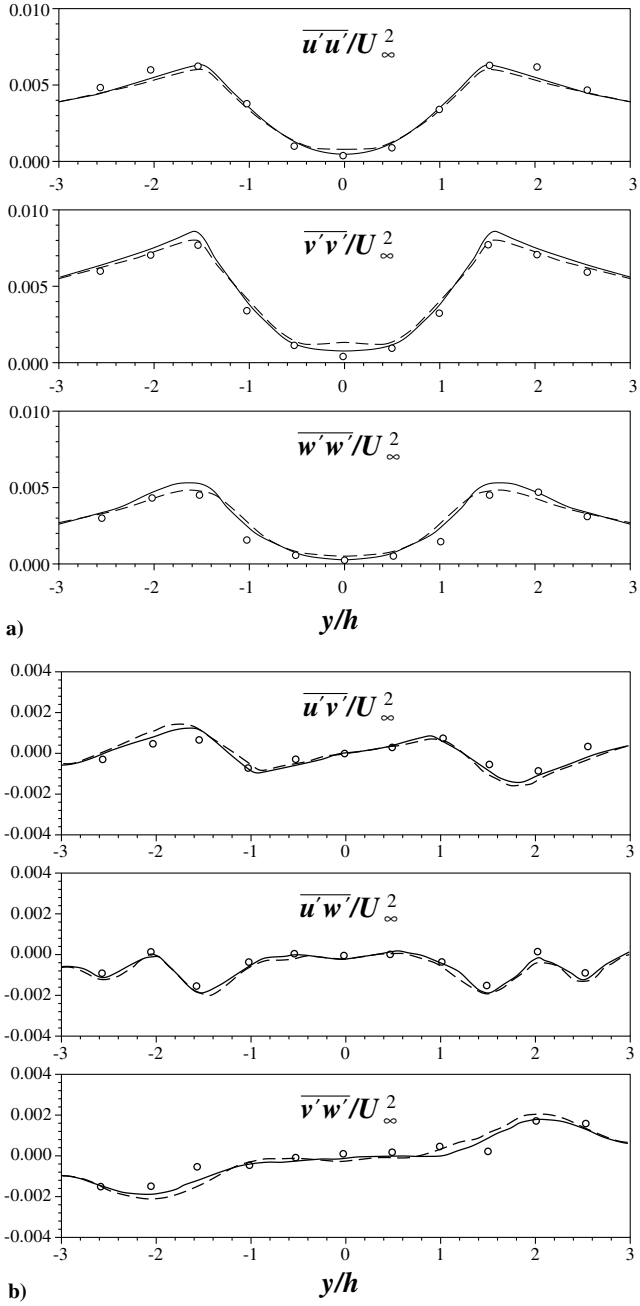

Fig. 12 Profiles of Reynolds stresses in the CFD case along the spanwise direction at $x/h = 10.5$ and $z/h = 0.75$: a) normal and b) shear. A solid line indicates mesh 2 and a dashed line indicates mesh 1. Symbols are from the experiment [5].

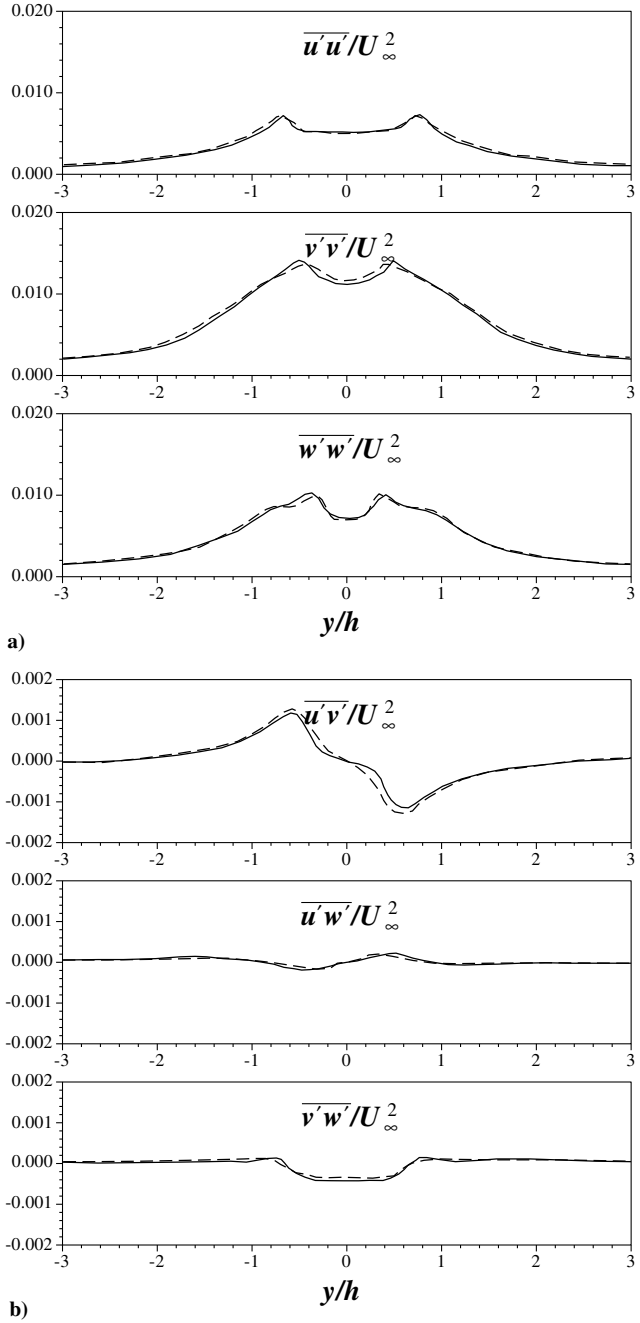

Fig. 13 Profiles of Reynolds stresses in the CFU case along the spanwise direction at $x/h = 10.5$ and $z/h = 0.75$: a) normal and b) shear. A solid line indicates mesh 2 and a dashed line indicates mesh 1.

In hydraulic applications, the negative pressure and pressure fluctuations generated by the longitudinal vortices and their interaction with end-wall turbulent boundary layers are of interest because they can cause unfavorable phenomena such as cavitation and broadband noise. In an axial hydraulic pump, the interaction between the convected vortical disturbances in the stator wake and the tip-leakage vortices generated by the downstream rotor blades can create an extremely complex flow and strongly affect the low-pressure events (see Fig. 1 for an illustration of vortex–rotor interaction). Figure 14 shows contours of time-averaged pressure for the CFD and CFU cases in the y–z plane at $x/h = 5$ obtained from the present LES. The spatial variations of the negative pressure relative to the mean values appear highly correlated with the longitudinal vortices and can potentially trigger cavitation events. In the farther downstream, negative pressure and intense pressure fluctuations are found in two distinct vortical regions close to the end wall in the CFD case, whereas they are concentrated in a single vortical region of larger size in the CFU case.

In the flow configuration illustrated in Fig. 1, the vortex pair in the CFD case is expected to be more effective in modulating the tip-leakage flow that develops close to the end wall. The same CFD configuration was used by Ma [6] in an experimental study of the effect of large-scale upstream disturbances on the tip-clearance flow in a linear cascade. On the other hand, the vortex pair in the CFU case is expected to affect a larger part of the rotor blade and trigger earlier transition of the blade boundary layer in the suction surface of the blade.

IV. Conclusions

Large-eddy simulations have been performed to examine the temporal and spatial evolution of longitudinal vortex pairs embedded in a turbulent boundary layer. An immersed boundary method is

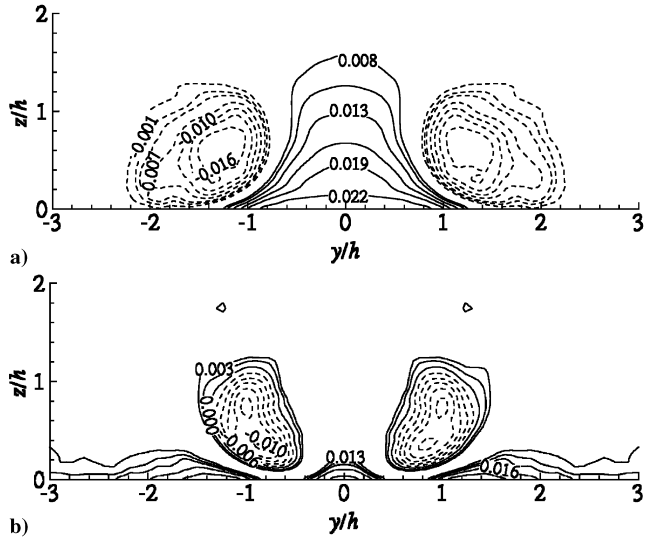

Fig. 14 Mean pressure contours in the cases in a y–z plane at $x/h = 5$. Thirteen levels in the ranges of $-0.016 \sim 0.022$ and $-0.010 \sim 0.018$ are shown, respectively, for the a) CFD and b) CFU cases. Negative values are dashed.

employed to simulate the pairs of wall-mounted half-delta wings that, depending on their relation orientation, generate longitudinal vortex pairs with flow between them directed either toward the end wall or away from the end wall. Results from the simulations show that the method is capable of capturing the complex flow features observed in the experiments [5,6,8–12]. Favorable agreement with experiments in terms of mean velocity and Reynolds stress profiles has been observed. The vortical structures generate intense turbulent fluctuations in the end-wall region as they convect downstream and expand in size. Vortices in the common-flow-down case thin the boundary layer, whereas those in the common-flow-up case thicken the boundary layer in the common flow region. Negative pressure, which can cause cavitation and acoustic noise in hydraulic turbomachines, is observed to be highly correlated with the development of vortex pairs. The unsteady flow data generated from the LES can be used to provide inlet boundary conditions that mimic important aspects of the upstream stator wakes in a tip-clearance flow simulation.

Acknowledgment

The authors acknowledge the support of the Office of Naval Research under grant N00014-99-1-0389, with Ki-Han Kim as program manager. Computer time was provided by Challenge Project grant C82 from the U.S. Department of Defense (DoD) High Performance Computing Modernization Program (HPCMP) through the Army Research Laboratory (ARL) Major Shared Resource Center (MSRC).

References

[1] Chang, P. K., *Control of Flow Separation. Energy Conservation, Operational Efficiency, and Safety*, McGraw–Hill, New York, 1976.

[2] Schoppa, W., and Hussain, F., "A Large-Scale Control Strategy for Drag Reduction in Turbulent Boundary Layers," *Physics of Fluids*, Vol. 10, No. 5, 1998, pp. 1049–1051.

[3] Soldati, A., Fulgosi, M., and Banerjee, S., "On the Use of Large Scale Vortical Streamwise Structures to Control Turbulence in Channel Flow," *Proceedings of the First International Symposium on Turbulence and Shear Flow*, edited by S. Banerjee and J. K. Eaton, Begell House, Santa Barbara, CA, 1999.

[4] Iuso, G., Onorato, M., Spazzini, P. G., and Cicca, G. M. D., "Wall Turbulence Manipulation by Large-Scale Streamwise Vortices," *Journal of Fluid Mechanics*, Vol. 473, 2002, pp. 23–58.

[5] Kuhl, D. D., "Near Wall Investigation of Three Dimensional Turbulent Boundary Layers," Master's Thesis, Department of Aerospace and Ocean Engineering, Virginia Polytechnic Institute and State University, Blacksburg, VA, Aug. 2001.

[6] Ma, R., "Unsteady Turbulence Interaction in a Tip Leakage Flow Downstream of a Simulated Axial Compressor Rotor," Ph.D. Thesis, Department of Aerospace and Ocean Engineering, Virginia Polytechnic Institute and State University, Blacksburg, VA, June 2003.

[7] Pearcy, H. H., "Shock-Induced Separation and Its Prevention by Design and Boundary Layer Control," *Boundary Layer and Flow Control*, edited by G. V. Lachmann, Pt. 4, Pergamon, New York, 1961, pp. 1277–1344.

[8] Spangler, J. G., and Wells, C. S. J., "Effects of Spiral Longitudinal Vortices on Turbulent Boundary Layer Skin Friction," NASA CR-145, Dec. 1964.

[9] Shabaka, I. M. M. A., Metha, R. D., and Bradshaw, P., "Longitudinal Vortices Imbedded in Turbulent Boundary Layers, Part 1: Single Vortex," *Journal of Fluid Mechanics*, Vol. 155, 1985, pp. 37–57.

[10] Metha, R. D., and Bradshaw, P., "Longitudinal Vortices Imbedded in Turbulent Boundary Layers, Part 2: Vortex Pair with 'Common Flow' Upwards," *Journal of Fluid Mechanics*, Vol. 188, 1988, pp. 529–546.

[11] Westphal, R. V., Eaton, J. K., and Pauley, W. R., "Interaction Between a Vortex and a Turbulent Boundary Layer in a Streamwise Pressure Gradient," *Turbulent Shear Flows*, edited by F. Durst, B. E. Launder, F. W. Schmidt, and J. H. Whitelaw, Springer–Verlag, New York, 1985, pp. 266–277.

[12] Pauley, W. R., and Eaton, J. K., "Experimental Study of the Development of Longitudinal Vortex Pairs Embedded in a Turbulent Boundary Layer," *AIAA Journal*, Vol. 26, No. 7, July 1988, pp. 816–823.

[13] Fadlun, E. A., Verzicco, R., Orlandi, P., and Mohd-Yusof, J., "Combined Immersed-Boundary Finite-Difference Methods for Three-Dimensional Complex Flow Simulations," *Journal of Computational Physics*, Vol. 161, No. 1, 2000, pp. 35–60.

[14] You, D., Mittal, R., Wang, M., and Moin, P., "Computational Methodology for Large-Eddy Simulation of Tip-Clearance Flows," *AIAA Journal*, Vol. 42, No. 2, Feb. 2004, pp. 271–279.

[15] Kim, J., Kim, D., and Choi, H., "An Immersed-Boundary Finite-Volume Method for Simulations of Flow in Complex Geometries," *Journal of Computational Physics*, Vol. 171, No. 1, July 2001, pp. 132–150.

[16] Ye, T., Mittal, R., Udaykumar, H. S., and Shyy, W., "An Accurate Cartesian Grid Method for Viscous Incompressible Flows with Complex Immersed Boundaries," *Journal of Computational Physics*, Vol. 156, No. 2, 1999, pp. 209–240.

[17] Mittal, R., and Iaccarino, G., "Immersed Boundary Methods," *Annual Review of Fluid Mechanics*, Vol. 37, 2004, pp. 239–261.

[18] You, D., Moin, P., Wang, M., and Mittal, R., "Study of Tip Clearance Flow in a Turbomachinery Cascade Using Large Eddy Simulation," Stanford University Department of Mechanical Engineering, Rept. TF-86, Stanford, CA, May 2004.

[19] Mittal, R., and Moin, P., "Suitability of Upwind-Biased Schemes for Large-Eddy Simulation of Turbulent Flows," *AIAA Journal*, Vol. 36, No. 8, 1997, pp. 1415–1417.

[20] Meneveau, C., Lund, T. S., and Cabot, W. H., "A Lagrangian Dynamic Subgrid-Scale Model of Turbulence," *Journal of Fluid Mechanics*, Vol. 319, 1996, pp. 233–242.

[21] Germano, M., Piomelli, U., Moin, P., and Cabot, W. H., "A Dynamic Subgrid-Scale Eddy-Viscosity Model," *Physics of Fluids*, Vol. A 3, No. 7, 1991, pp. 1760–1765.

[22] Akselvoll, K., and Moin, P., "Large Eddy Simulation of Turbulent Confined Coannular Jets and Turbulent Flow Over a Backward Facing Step," Stanford University Department of Mechanical Engineering, Rept. TF-63, Stanford, CA, Feb. 1995.

[23] Lund, T. S., Wu, X., and Squires, K. D., "Generation of Turbulent Inflow Data for Spatially-Developing Boundary Layer Simulations," *Journal of Computational Physics*, Vol. 140, No. 2, 1998, pp. 233–258.

X. Zhong
Associate Editor